



In-situ selective laser heat treatment for microstructural control of additively manufactured Ti-6Al-4V

Reza Esmaeilzadeh^{a,*}, Milad Hamidi-Nasab^a, Charlotte de Formanoir^a, Lucas Schlenger^{a,1}, Steven Van Petegem^{b,2}, Claire Navarre^{a,3}, Cyril Cayron^a, Nicola Casati^c, Daniel Grolimund^{d,4}, Roland E. Logé^{a,5}

^a Thermomechanical Metallurgy Laboratory – PX Group Chair, École Polytechnique Fédérale de Lausanne (EPFL), CH-2002 Neuchâtel, Switzerland

^b Structure and Mechanics of Advanced Materials, Photon Science Division, Paul Scherrer Institut, Forschungsstrasse 111, 5232 Villigen, Switzerland

^c MS beamline, Swiss Light Source, Paul Scherrer Institut, Forschungsstrasse 111, 5232 Villigen, Switzerland

^d MicroXAS beamline, Swiss Light Source, Paul Scherrer Institut, Forschungsstrasse 111, 5232 Villigen, Switzerland

ARTICLE INFO

Keywords:

Laser Powder Bed Fusion (LPBF)
Selective Laser Heat Treatment (SLHT)
Martensite decomposition
Operando X-ray diffraction
Finite Element Simulation (FEM)

ABSTRACT

As-built Laser Powder Bed Fusion (LPBF) Ti-6Al-4V typically exhibits a fully acicular α' -martensite microstructure, and requires post-process heat treatment in order to decompose the martensite and achieve sufficient ductility. In the present study, we demonstrate a simple concept based on *in-situ* Selective Laser Heat Treatment (SLHT) that can effectively alter the microstructure and activate the decomposition of the α' -martensite into a lamellar $\alpha + \beta$ microstructure within a short time scale (~ 30 s). SLHT consists of multiple rescanning of the printed part, with low energy density, triggering solid-state phase transformations. *Operando* X-ray diffraction has been performed on cuboid and thin wall geometries, and was augmented by thermal finite element simulations. Upon SLHT, a gradual formation of the β phase as well as an α' peak narrowing trend have been evidenced through X-ray diffraction, as an indication of the diffusional nature of α' -martensite decomposition. Moreover, through fine tuning of the process parameters at the final stage of SLHT, a controlled temperature evolution during cooling was achieved, leading to preservation of the β phase, a product of the decomposition, down to room temperature. Complementary microstructural characterizations via EBSD, SEM, and TEM confirm the presence of a lamellar $\alpha + \beta$ microstructure after SLHT. Our results evidence, for the first time, the fast kinetics of α' -martensite decomposition under *in-situ* SLHT. The approach is meant to be implemented at selected locations during the LPBF process, avoiding time-consuming post processing steps, and leading to composite-like, architected microstructures.

1. Introduction

The game-changing design freedom offered by Additive Manufacturing (AM) enables the production of customized products that would be unachievable through conventional manufacturing techniques [1]. Among various AM methods, Laser Powder Bed Fusion (LPBF) is the most well-known technique for the production of metallic parts. This process is based on the consecutive melting of deposited layers of

powder on top of already solidified material, utilizing a laser heat source to obtain a 3-dimensional geometry [2,3]. The primary objective in LPBF is to produce fully dense parts with minimum porosity content. This can be achieved through an optimization of the processing parameters (so-called processing window), i.e. laser power, scanning speed, hatching distance, etc. The density optimization for most metallic materials is often restricted within a narrow processing window, thus leaving little room for microstructural control in the as-built state [2,4,

* Corresponding author.

E-mail address: reza.esmaeilzadeh@epfl.ch (R. Esmaeilzadeh).

¹ <https://orcid.org/0009-0009-1062-6369>

² <https://orcid.org/0000-0002-3015-7725>

³ <https://orcid.org/0000-0001-6510-0190>

⁴ <https://orcid.org/0000-0001-9721-7940>

⁵ <https://orcid.org/0000-0002-9761-7538>

5]. Additionally, due to the fast heating and cooling occurring during LPBF, the pile-up of residual stresses and frequent formation of non-equilibrium phases are often inevitable. As a result, as-built parts require time-consuming post-process heat treatments to meet standards for part quality, which reduces the overall efficiency of LPBF [2].

The Ti-6Al-4V alloy features high strength and corrosion resistance as well as acceptable ductility and fracture toughness, with widespread applications in bio-medical, automobile and aeronautical industries [6–8]. At thermodynamic equilibrium, this material presents a mixture of hcp (α) and bcc (β) phases stable at room temperature, providing balanced strength and ductility. However, the microstructure of LPBF parts is directly inherited from their specific thermal history [9]. The high cooling rates (10^3 to 10^6 K/s) experienced during LPBF favor a diffusionless transformation from the β phase to the non-equilibrium acicular α' -martensite [10,11]. Typically, Ti-6Al-4V parts fabricated via LPBF present a high strength at the expense of ductility, which can be attributed to their martensitic microstructure [12,13]. Therefore, several studies have focused on performing post-process heat treatments to decompose the α' -martensite into thermodynamically stable $\alpha + \beta$, in order to satisfy the standards for mechanical properties [10,14,15]. Few studies exist, that demonstrate approaches leading to a lamellar $\alpha + \beta$ microstructure in as-built LPBF condition, either via *in-situ* decomposition of martensite ($\alpha' \rightarrow \alpha + \beta$) or via slow cooling from the high temperature β phase ($\beta \rightarrow \alpha + \beta$). Xu et al. [16] have shown that a proper selection of energy densities combined with large layer thickness (60 μm) and Focal Offset Distance (FOD) (2 mm) could result in *in-situ* decomposition of α' -martensite into fully lamellar $\alpha + \beta$ in the Heat Affected Zone (HAZ), maintaining a yield strength above 1100 MPa while reaching an excellent elongation of 11.4 %. In another study [17], they concluded that factors affecting the heat build-up during the print in the already solidified layers, such as large geometries, fine support structures, short inter-layer time, and large layer thicknesses, could promote *in-situ* martensite decomposition in the HAZs. However, key processing conditions such as laser beam profile and spot size were not disclosed. Barriobero-Vila et al. [18] employed a small hatching distance of 40 μm to increase the laser exposure time, promoting a so-called intensified heat treatment upon printing operated at FOD:2 mm. Although the approach led to $\alpha + \beta$ structure due to the heat build-up, martensite remained present in the few last layers. Zafari et al. [19] demonstrated that the employment of pulse mode laser beam with careful selection of the parameters with energy densities above $70 \text{ J} \cdot \text{mm}^{-3}$ can trigger the α' -martensite decomposition mainly in the bulk, but not in a few top layers. All these findings can be categorized in the *in-situ* martensite decomposition scenario which is based on the formation of α' -martensite ($\beta \rightarrow \alpha'$) followed by its decomposition ($\alpha' \rightarrow \alpha + \beta$) due to the heat build-up induced by successive layer depositions. Recently, Chen et al. [20] demonstrated that the waiting time between each layer can be adjusted to promote heat accumulation, to generate the lamellar $\alpha + \beta$ structure upon slow cooling from the β phase. This approach was also obtained at ambiguous off-focus laser operating condition. Still, the vast majority of LPBF Ti-6Al-4V parts exhibit a martensitic microstructure, and the above-mentioned approaches are mainly limited to very specific and sometimes undisclosed processing conditions, which cannot necessarily be applied to all circumstances/geometries. Therefore, they are mostly empirical and lack a rationale behind the choice of a given parameter set. This is mostly related to an insufficient understanding of the physics behind martensite decomposition. Most of the efforts so far were focused on the post-mortem microstructural analysis, and on numerical modelling demonstrating specific temperature regimes operating in the HAZs and related to the α' -martensite decomposition during the print [20–23].

Operando synchrotron experiments have recently revolutionized the monitoring of laser-material interactions, as they provide key information at a time resolution compatible with the LPBF process [24–30]. Thanks to fast acquisition detectors and the development of a dedicated

LPBF machine adaptable to synchrotron beamlines, Hocine et al. [24] used *operando* diffraction to successfully track the phase evolution of α' and β phases during LPBF processing of Ti-6Al-4V. They showed that the longevity of the β phase is a function of energy density as well as of the scanning vector length. The β phase has a longer lifetime if the scanning vector length is decreased, which not only affects the thermal cycles and cooling rate, but also the final microstructure and potentially the corresponding mechanical properties. The local average temperature evolution acquired from *operando* experiments has been used to calibrate and compare different numerical simulation models and create a basis for large-scale simulations of the process [24,31].

Based on the abovementioned literature, a better understanding and quantification of the (LPBF-induced) α' -martensite decomposition is needed. We therefore investigate, in this study, the *dynamics* of the α' -martensite decomposition by means of *operando* synchrotron X-ray diffraction. We introduce a highly flexible tool, called *in-situ* Selective Laser Heat Treatment (SLHT), to control the microstructure of selected zones of the LPBF part. Unlike the existing approaches for microstructural control in Ti-6Al-4V, SLHT does not necessarily require the use of very specific melting processing parameters or geometries. While other aspects of the printed parts are often controlled separately, e.g. density with respect to the geometry, the microstructure can be subsequently and independently controlled at a very local scale via SLHT.

The *operando* experiments were conducted at diffraction synchrotron beamlines, using cuboid samples in reflection mode, and thin walls in transmission configuration, to shed light on the applicability of SLHT for any given geometry. The time evolution of the β phase as a function of the laser parameters and corresponding thermal history was evidenced in the diffraction data. Moreover, the evolution of the β phase upon martensite decomposition was detected down to 250 μm below the top surface of a thin wall, providing the first direct observation of its fast kinetics, and demonstrating the possibility of building 3D composite-like microstructures. A finite element temperature field simulation was also employed to investigate the temperature evolution upon SLHT as a function of processing parameters and geometry. As SLHT can be applied to any given material and geometry, the derived temperature data from *operando* X-ray diffraction was then used to further calibrate the numerical simulation, allowing to design offline SLHT routes. The effects of heat treatment parameters and cooling rates are discussed. Complementary microstructural characterization via SEM, EBSD, and TEM were performed to provide evidence of the occurrence of decomposition in both geometries, demonstrating the efficiency of SLHT as a reliable tool for finely tuning the microstructure. Supported by a combination of *operando* experiments and numerical simulations, our findings suggest that SLHT can expand the range of possibilities offered by LPBF in terms of microstructure tailoring. In the case of Ti-6Al-4V, martensite decomposition can occur sufficiently deep underneath the laser treated surface to not be affected by the subsequent addition of LPBF layers. The SLHT strategy therefore allows the creation of 3D architected (or composite-like) microstructures, in the as-built state.

2. Experimental method

2.1. Materials and fabrication

Commercial gas-atomized Ti-6Al-4V ELI (grade 23) powder provided by (AP&C, GE Additive, Canada) is used in this study. The powder has a Particle Size Distribution (PSD) of $D_{90} = 47 \mu\text{m}$, $D_{50} = 35 \mu\text{m}$, and $D_{10} = 21 \mu\text{m}$ (according to ASTM B214-16), and a chemical composition listed in [supplementary Table S1](#). The feedstock powder shown in [supplementary Fig. S1](#) features mainly spherical particles.

The printing was performed utilizing a mini-LPBF machine, specifically developed for *operando* experiments at synchrotron beamlines. A detailed description of the machine functionalities can be found in [32]. A set of optimized processing parameters (laser power: 80 W, scanning

speed: 1200 mm/s, Hatching Distance (HD): 60 μm , layer thickness of 20 μm , laser spot radius (ω): 15 μm ($1/e^2$) was used for printing parts with minimum porosity content (relative densities higher than 99.8 %). Two different geometries, i.e. cuboid and thin walls, were printed separately on $12 \times 12 \text{ mm}^2$ grade 5 Ti base plates without preheating, for reflection and transmission mode *operando* experiments, respectively. Cuboid samples (length: 4 mm, width: 2 mm) were built using 25 lines per layer whereas thin wall shapes were obtained employing 4-line tracks. For both geometries, bidirectional parallel lines with a scanning vector length of 4 mm were used for the melting of each layer, until a certain height ($\sim 1.7 \text{ mm}$) was reached. The *operando* experiments were then initiated on the solid parts in absence of powder.

2.2. Selective laser heat treatments (SLHTs)

After the built job, the powder was removed, and the SLHTs were done using the prescribed mini-LPBF machine under dynamic Ar atmosphere, to maintain the oxygen level below 0.1 %. A negatively defocused beam was used, i.e. the plane of focus was below the top surface of the part ($\omega=182 \mu\text{m}$). Multiple rescanning of the top surface was performed in order to activate solid state phase transformations. The laser spot size was measured using a Focus Beam Profiler (FBP-1KF) CMOS type camera provided by CINOGY, operating the RayCi software as demonstrated in [supplementary Fig. S2](#). In the present study, the selection of the processing parameters has been done using the concept of Normalized Enthalpy (NE) [33–35] expressed in Eq. (1):

$$\Delta\bar{H} = \frac{\Delta H}{\Delta h} = \frac{\alpha P}{\rho(C\Delta T + L_m)\sqrt{\pi\omega^3 V D}} \quad (1)$$

where the averaged enthalpy of the system is normalized by the enthalpy at melting point as $\frac{\Delta H}{\Delta h}$, with α the absorptivity of the material, P the laser power (W), ρ the material density ($\frac{\text{kg}}{\text{m}^3}$), C the specific heat ($\frac{\text{J}}{\text{kg}\cdot\text{K}}$), ΔT the temperature difference between the melting and initial condition (K), L_m the latent heat of melting ($\frac{\text{J}}{\text{kg}}$), ω the laser spot radius (m), V the laser scanning speed ($\frac{\text{m}}{\text{s}}$), and D the thermal diffusivity ($\frac{\text{m}^2}{\text{s}}$).

One necessity of SLHT is to remain below the melting point, therefore, the laser parameters were adjusted accordingly to have $\Delta\bar{H}$, which theoretically should prevent the material from melting. The material properties used for the $\Delta\bar{H}$ calculation as well as the SLHT parameters are presented in [Table 1](#) and [Fig. 1](#), respectively. The absorptivity of the as-printed parts prior to heat treatment is taken to be 45 % at 1070 nm wavelength as measured by a spectrophotometer (Perkin Elmer Lambda900) device. Other material properties were derived from literature.

The chosen SLHT for the cuboid specimens consists of 25 unidirectional lines with a hatching distance of 80 μm . In order to reduce the cooling rate at the end of the heat treatment, some specimens were subjected to additional SLHT cycles ([Fig. 1\(b\)](#)) with a so-called modulation (i.e. changing laser parameters) resulting in a gradual decrease in $\Delta\bar{H}$. The changing cycles started with an increment of 100 mm/s in the scanning speed until it reached 5000 mm/s at 40 W laser power. Thereafter, the laser power was gradually decreased down to 15 W by steps of 1 W, while maintaining the maximum scanning speed of

5000 mm/s. Regarding the thin wall geometries, only 1-line track was rescanned multiple times at 35 W and 1500 mm/s, after which modulation was applied as described and shown in [Fig. 1\(c\)](#). All laser parameters were adjusted via the WeldMARK (Raylase GmbH, Germany) platform. The total duration of the SLHT cycles was kept around 30 s for all experiments.

2.3. Operando synchrotron X-ray diffraction

The *operando* experiments were done in reflection and transmission mode using the already described mini-LPBF machine installed at the Materials Science (MS) and MicroXAS beamlines, respectively (Swiss Light Source (SLS)). The mini-LPBF is placed on a tilting stage that can be adjusted depending on the configuration (transmission or reflection) as shown in [Fig. 2](#). It has two glassy carbon windows at the back and front side of the printing chamber, which are transparent to high-energy X-rays. The X-ray beam enters through the back window and interacts with the printed part [32]. The diffraction rings then exit through the front window, and get captured by an ultrafast single photon EIGER 1 M detector placed outside of the chamber [39]. 36,000 patterns were recorded using a 1 kHz acquisition frequency resulting in a temporal resolution of 1 ms. The *operando* SLHT cycles were performed on as-built samples after removal of powder ([Fig. 2\(b, d\)](#)).

At the MS beamline, the X-ray energy was set to 12.6 keV and the detector was placed at a 24.5 mm distance with respect to the front edge of the base plate, spanning the angular range of 10–55° in reflection mode. Given the 15° tilting angle of the machine in regard to the incident X-ray beam, the diffracted patterns provide information over a small volume with a projection area of 300 $\mu\text{m} \times 280 \mu\text{m}$ (horizontal \times vertical) on the top surface of the cuboid specimens ([Fig. 2\(b\)](#)).

At the MicroXAS beamline, an X-ray beam with a 17.18 keV energy was focused over an illuminated area of 40 $\mu\text{m} \times 10 \mu\text{m}$ (horizontal \times vertical) on the thin wall geometry ([Fig. 1\(d\)](#)). The mini-LPBF machine had a slight tilting of 2° with respect to the incoming X-ray beam. The detector was placed at a distance of 80 mm from the edge of the base plate covering the angular range of 10–45°. In both configurations, several SLHT cycles were conducted, each on a fresh as-built state, to investigate the phase evolution with respect to the SLHT parameters. The X-ray beam was positioned at the center of the top surface for cuboid specimens, while for the transmission experiments on thin walls, it was placed at 50 μm , 150 μm , and 250 μm below the top surface, to investigate the phase evolution at different depths. Additionally, spatially resolved diffraction patterns with 5 s exposure time were acquired over a rectangular area of $3 \times 0.7 \text{ mm}^2$ to capture the phase distribution with better statistics in both geometries. The captured 2D diffraction rings were azimuthally integrated via an established Python library (PyFAI) to generate 1D diffraction patterns [40]. An in-house developed MATLAB script was employed for peak analysis. Local temperatures averaged over the X-ray probed volume were derived from peak shifting assuming a superior contribution of thermal expansion and contraction on the lattice strain compared to residual stresses and compositional changes. Accordingly, based on temperature-related thermal expansion coefficients [41], temperature values were indirectly calculated from changes in the lattice strain.

2.4. Numerical simulation

Finite Element Method (FEM) simulations were performed using the Abaqus plug-in AM modeler to investigate the temperature evolution during the *in-situ* SLHT. The general heat equation stated in [Eq. \(2\)](#) is solved implicitly at each increment.

$$\rho C_p \frac{\partial T}{\partial t} = \frac{\partial}{\partial x} \left(k \frac{\partial T}{\partial x} \right) + \frac{\partial}{\partial y} \left(k \frac{\partial T}{\partial y} \right) + \frac{\partial}{\partial z} \left(k \frac{\partial T}{\partial z} \right) \quad (2)$$

where ρ is the temperature-dependent density of the material, C_p the

Table 1

Material properties of Ti-6Al-4V used as input for Normalized Enthalpy calculations ([Eq. \(1\)](#)).

| Bulk Absorptivity | Latent heat of melting (J/kg) | Density (kg/m ³) | Thermal Diffusivity at room temperature (m ² /s) | Specific heat at room temperature (J/kg.K) |
|-------------------|-------------------------------|------------------------------|---|--|
| 0.45 | 2.9×10^5 [36] | 4.246×10^3 [37] | 2.7×10^{-6} [38] | 534 [38] |

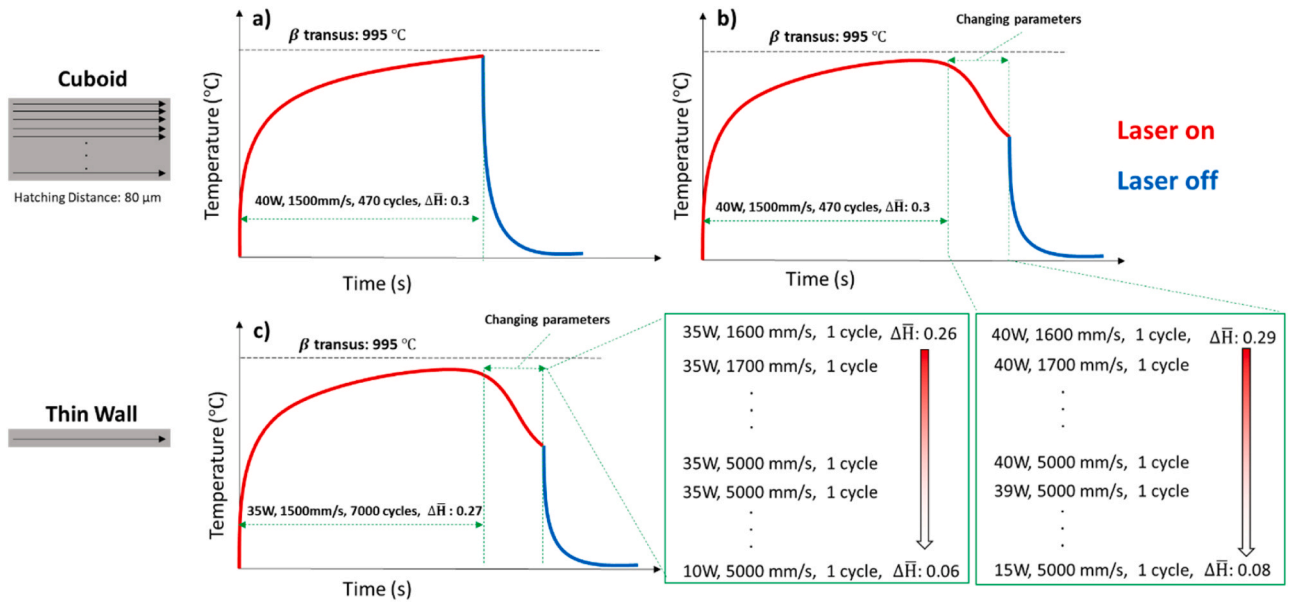


Fig. 1. Schematic of the SLHT parameters for cuboid and thin wall geometries. SLHT cycles with a) constant laser parameters, b) constant plus changing parameters (modulation) at the end, for cuboid geometry, and c) SLHT cycle with modulation for a thin wall geometry. The insets show the selected changing laser parameters, allowing to reduce the cooling rate at the end of the heat treatment.

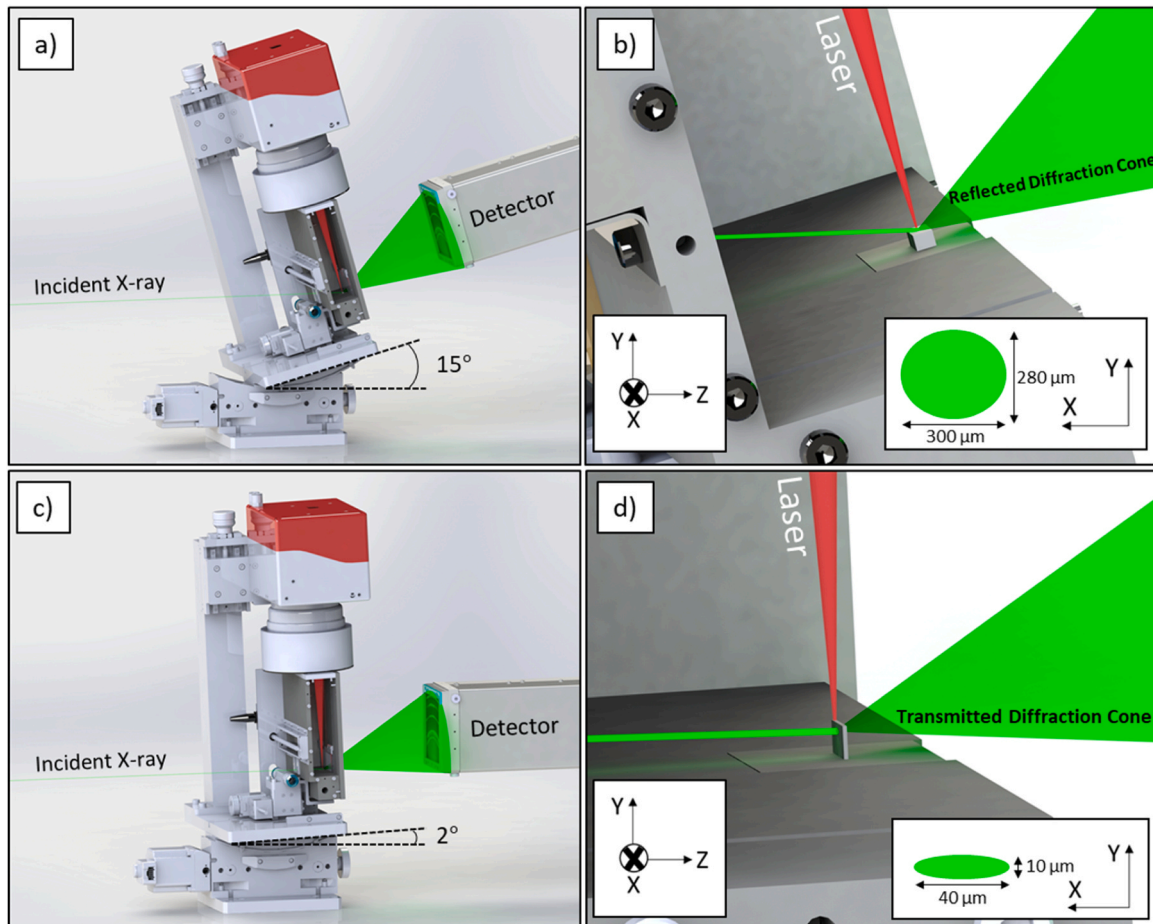


Fig. 2. Schematic of the mini-LPBF machine placed at synchrotron beamlines for *operando* experiments. a) and b) reflection mode at MS beamline, c) and d) transmission configuration at MicroXAS beamline. The insets in b) and d) show the projection area of the X-ray beam on the samples with respect to XY plane.

temperature-dependent specific heat capacity, T the temperature, t the time, and k the temperature-dependent thermal conductivity. Radiation heat losses are implemented using the Stefan-Boltzmann law as expressed in Eq. (3):

$$q_{\text{rad}} = \varepsilon \sigma (T_s^4 - T_\infty^4) \quad (3)$$

where ε is the surface emissivity, σ the Stefan-Boltzmann constant, T_s the surface temperature and T_∞ the ambient temperature. Convection heat losses are modeled using a film coefficient from Eq. (4):

$$q_{\text{con}} = h(T_s - T_\infty) \quad (4)$$

where h is the film coefficient, T_s the surface temperature, and T_∞ the ambient temperature.

Since the AM modeler does not allow for the direct implementation of a Gaussian heat source, a modified Goldak heat source developed by Zhang [42] is implemented as presented in Eq. (5):

$$Q(x, y, z, t) = \frac{2\alpha P}{R_0^2 O_{PD} \sqrt{\pi}} \exp \left[- \left(\frac{x^2}{R_0^2} + \frac{y^2}{R_0^2} + \frac{z^2}{O_{PD}^2} \right) \right] \quad (5)$$

Where α is the absorptivity of the material, R_0 is the $1/e$ spot radius ($\omega=182 \mu\text{m}$) of the laser beam and O_{PD} is the optical penetration depth of the laser beam in the material. The O_{PD} is set to be $1 \mu\text{m}$ as it is small enough to effectively result in a surface heat flux while still fulfilling the requirement of the AM modeler plugin to be a volume heat flux. The mesh size description can be found in Supplementary Fig. S3.

All the nodes in the simulated domain were initialized with a temperature of 300 K. Radiation and convection heat losses described by Eqs. (3) and (4) are applied to the top and side surfaces of the sample, as well as to the free top surface of the substrate. The remaining boundaries of the domain are considered adiabatic. The temperature dependent specific heat capacity, density, and thermal conductivity are taken from Mills [43]. The emissivity is taken to be 0.26 as measured by Rodriguez et al. [44], and the convection heat transfer coefficient was considered as $15 \frac{\text{W}}{\text{m}^2\text{K}}$ [45]. The simulation is done using the same SLHT parameters as for *operando* experiments described in Section 2.2.

In order to compare simulated temperatures with those measured from the *operando* experiments, the reported temperatures from the FEM are post processed to derive weighted average nodal temperatures based on the Gaussian distribution of the X-ray beam.

2.5. Microstructural analysis

The microstructural analysis of the powder and printed parts was mainly conducted using a Scanning Electron Microscope (SEM) (ZEISS GeminiSEM450) equipped with an Energy Dispersive X-ray Spectroscopy (EDS) and Electron Backscatter Diffraction (EBSD) detectors (CMOS Symmetry camera, Oxford Instruments). The samples in as-built and SLHTed conditions were mounted in a resin and polished down to $3 \mu\text{m}$ by a monocrystalline diamond suspension followed by a final polishing utilizing a mixture of 5:1 OP-S ($0.25 \mu\text{m}$) and hydrogen peroxide. The porosity content was measured via the ImageJ software with FIJI extension, treating Optical Microscopy (OM) (Leica DM6000M) images having less than 0.2 % porosity contents as shown in supplementary Fig. S4. The same polishing procedure was applied to the top surface of the cuboid samples for EBSD analysis. Slight chemical etching was performed to remove the oxide layer and reveal the microstructure via Kroll's (2 ml HF- 6 ml HNO₃- 96 ml H₂O) reagent. EBSD maps were acquired at 25 kV and 10 nA with step sizes of 0.6 and $0.1 \mu\text{m}$ using AZtec (Oxford) software and were post treated with the Aztec Crystal (Oxford) plug-in. MTEX MATLAB scripts [46] were employed to reconstruct the prior parent β phase based on the Burgers Orientation Relationships (BORs), and considering a misorientation threshold of 5° . Complementary microstructural analysis was obtained via Transmission Electron Microscopy (TEM) (TECNAL, OSIRIS, FEI).

The lamellas were prepared using a gallium-source Focused Ion Beam (FIB) lift-out method. Scanning Transmission Electron Microscopy (STEM) mode imaging was carried out on the top surface of a SLHTed cuboid sample, using a High Angle Annular Dark Field (HAADF) detector operating at 200 kV, together with EDS analysis. The TEM images were treated via an industry standard Digital Micrograph platform.

3. Results and discussion

3.1. Cuboid geometry

3.1.1. Numerical simulation

Prior to the *operando* experiments, FEM numerical simulations were performed on a cuboid geometry, as described in Section 2.4., to understand the effect of SLHT parameters on the temperature field and cooling rates. Fig. 3. displays a snapshot of the simulated temperature field during the last scanning passes. Note that for the sake of computational time, reduced time steps (0.13 ms) were only considered from $t = 28 \text{ s}$.

Two heat treatment conditions were considered:

- without modulation (solid red line), i.e. with a constant laser parameter set from the beginning to the end of the SLHT;
- with modulation (solid blue line), i.e. the same heat treatment plus additional cycles for reducing the cooling rate.

Both curves follow equivalent thermal cycles until $t \sim 29.2 \text{ s}$, however, in the presence of modulation, the temperature gradually decreases until $t \sim 31.6 \text{ s}$ whereas in the absence of modulation, it suddenly drops at $t \sim 29.2 \text{ s}$. The resulting cooling rate changes accordingly, as shown in dashed lines for cases a) and b) in Fig. 3. It can be concluded that a step-wise decrease in ΔH in the last SLHT cycles is effective in reducing the cooling rate drastically. Since the occurrence of martensitic phase transformation is heavily dependent on the cooling rate [47], SLHT can be defined with or without modulation, such as to inhibit or not the transformation, and this can be monitored by means of *operando* XRD.

3.1.2. Operando X-ray diffraction

Fig. 4. shows the *operando* XRD data taken in reflection configuration upon *in-situ* SLHT on a cuboid sample. The $300 \times 280 \mu\text{m}^2$ X-ray beam generates an average information over a probed volume positioned in the center of the top surface. When the laser approaches the vicinity of the X-ray beam, the changes in the lattice structure and phase transformations induced by the laser are detected in the diffraction pattern. For constant laser parameters, each line track takes $\sim 2.7 \text{ ms}$, and a full surface scanning lasts $\sim 67 \text{ ms}$. Therefore, a 1 ms time resolution for successive diffraction frames is sufficient to capture the phase evolution during the SLHT cycles. A zoomed view of the low angle diffraction planes is shown to better represent the phase evolution of the high intensity peaks. The diffraction data over a wider angular range can be found in supplementary Fig. S5. Fig. 4 compares the *operando* XRD of SLHT without modulation (case a) and with modulation of laser parameters (case b). At time zero, the initial phase is hexagonal α/α' without any detectable β phase. Upon SLHT, the diffraction peaks of the $\{0002\}$ and $\{101\}$ planes of α/α' shift towards smaller angles over time. This effect is due to the thermal expansion of the lattice during SLHT, as reported in [24,48]. The first evidence of β phase formation starts appearing at $t \sim 5 \text{ s}$. Although there are some fluctuations in the intensity of the β phase over time, the average intensity of the $\{011\}_\beta$ peak gradually increases until the end of the heating cycle ($t \sim 29.2 \text{ s}$). At this time, the cooling cycles start, therefore, the lattice experiences a thermal contraction resulting in peak shifting to higher diffraction angles. This peak shifting is observable for both $\{0002\}_{\alpha/\alpha'}$ and $\{101\}_{\alpha/\alpha'}$ peaks as well as for the $\{011\}_\beta$ peak. In case of SLHT without modulation (Fig. 4

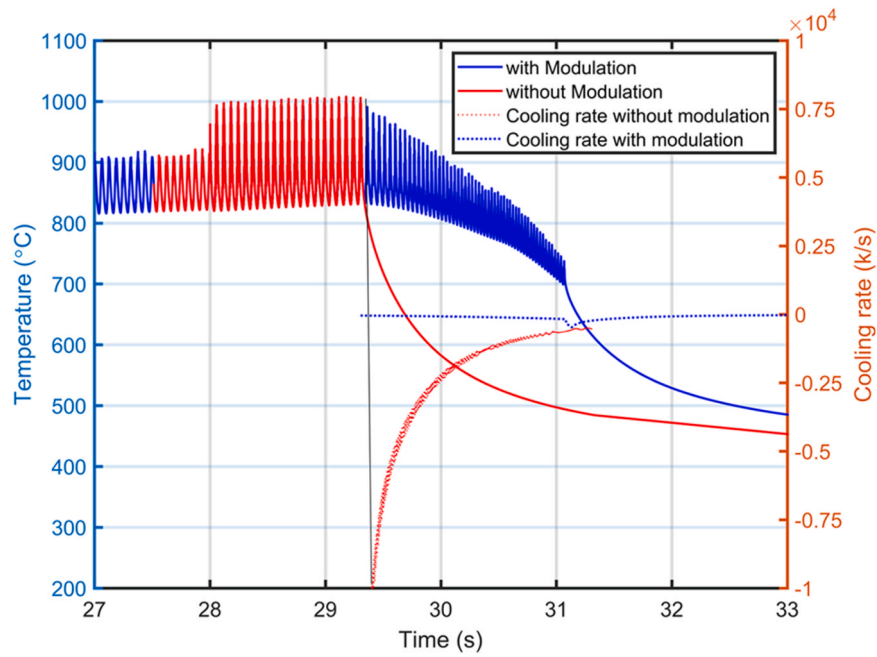


Fig. 3. FEM simulation of temperature evolution at the top surface of the cuboid geometry in the presence and absence of modulation in parameters upon *in-situ* SLHT.

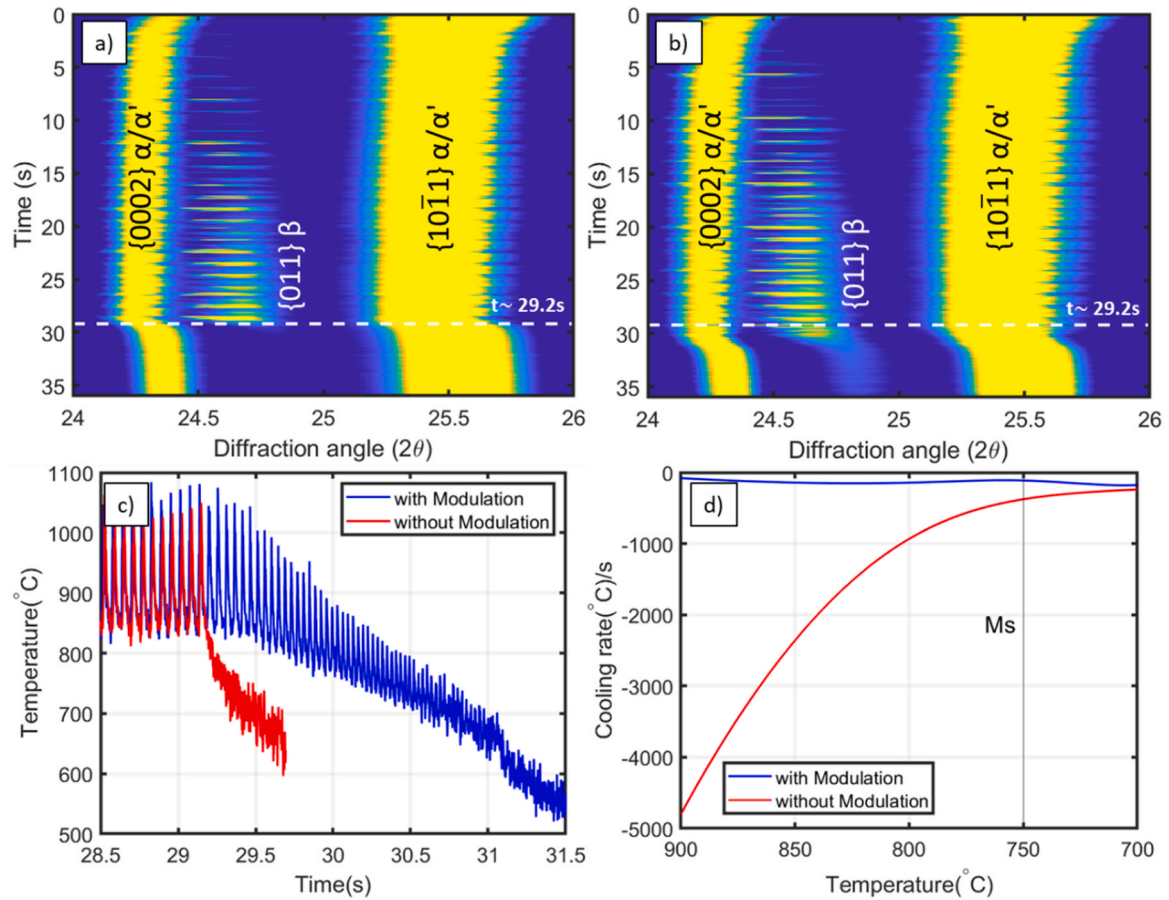


Fig. 4. Operando X-ray diffraction of SLHT a) without modulation, b) with modulation. c) temperature and d) cooling rate evolution of the last cycles of SLHT with (in blue) and without modulation (in red). (For interpretation of the references to color in this figure legend, the reader is referred to the web version of this article.)

(a)), the β phase disappears upon its reverse transformation to α -martensite, whereas, in case (b) with modulation (Fig. 4(b)), the β phase is partially retained after the end of SLHT cycles. Since both α and α' have similar hexagonal crystal structures, the presence of β together with α/α' diffraction peaks constitute the main evidence of a retained decomposition of the α' -martensite upon the SLHT modulated cycles.

The *operando* experiments elucidate a significant difference in the retainment of the β phase arising from the α' -decomposition in the presence and absence of cooling rate modulation. Assuming an isotropic thermal behavior of the β phase, temperatures are indirectly derived by tracking the peak shift of the $\{011\}_\beta$ over time, for both cases (a) and (b), as shown in Fig. 4(c). The inferred temperature evolutions were examined for the last SLHT cycles, to evaluate the corresponding cooling rates (Fig. 4(d)). In Fig. 4(c), the temperature evolution resulting from SLHT without modulation is presented as a red curve while the blue curve refers to SLHT with modulation. Comparable to the simulation data (Fig. 3), as long as constant parameters are used, the temperature evolution follows the same path for both cases. The difference becomes evident at $t = 29.2$ s where the SLHT cycles end in case (a), while the modulation in SLHT parameters starts in case (b) and ends at $t = 31$ s. The gradual decrease in temperature until the last, low ΔH , SLHT cycle in case (b) implies that the controlled cooling rate has led to preservation of the β phase. Fig. 4(d) shows the cooling rate derived from the temperature evolution data presented in Fig. 4(c), by fitting a smoothed polynomial curve on the weighted average temperatures. It can be seen that applying the modulation for case (b) has reduced the effective average cooling rate by 3 orders of magnitude compared to case (a). Note that the difference in cooling rate becomes smaller as the temperature drops. Considering the martensite start temperature (M_s) at around 750°C for Ti-6Al-4V [20], the cooling rate is ~ 3 times smaller at this temperature for case (b) compared to case (a). This reduction in cooling rate has preserved some β formed during SLHT, i.e. it prevented the reverse formation of α' -martensite. It is noted that the absolute temperature values in both experimental and simulation data are in relatively good agreement. The exact experimental values can be biased due to the potential contributions of compositional changes and residual stresses on the measured lattice strains, as commented already in Section 2.3. Upon relatively short SLHT and partial decomposition of the α' -martensite, these sources of bias appear limited, since measurements and simulations are relatively in accordance with each other. Overall, the average values of the experimental data are in the acceptable range

for the α' decomposition, i.e. not exceeding the β transus ($\sim 995^\circ\text{C}$) [49]. For longer SLHT durations, the experimental approach would potentially result in inconclusive temperature values due to significant compositional changes.

Fig. 5(a), and (b) present the single XRD patterns taken from the *ex-situ* scanning of the cuboid sample in the as-built and SLHTed state for both cases (a), and (b). Note that the 1D XRD patterns were taken by summing 20 single patterns acquired at different positions for better statistics. The as-built sample contains a fully hexagonal α' -martensitic structure which has been repeatedly reported in the literature as the dominant phase after LPBF processing [50]. In the case of SLHTed samples, the $\{110\}_\beta$ peak is clearly more pronounced in case (b), as shown in blue in Fig. 5(b). Only small traces of β phase can be identified for case (a). The critical cooling rate of ~ 410 K/s has been widely reported for conventional thermal processes to obtain a fully martensitic microstructure in Ti-6Al-4V [47]. However, in the field of laser

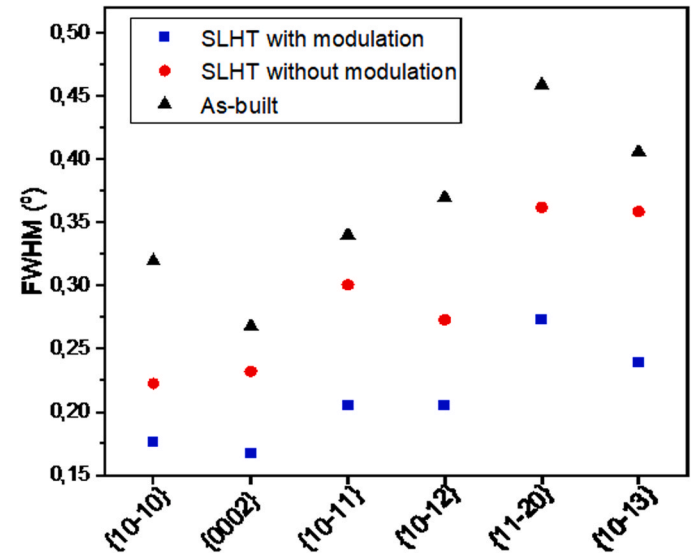


Fig. 6. FWHM values taken from *ex-situ* diffraction patterns of the hexagonal α/α' phase after SLHT with modulation (blue), without modulation (red), and as-built state (black). (For interpretation of the references to color in this figure legend, the reader is referred to the web version of this article.)

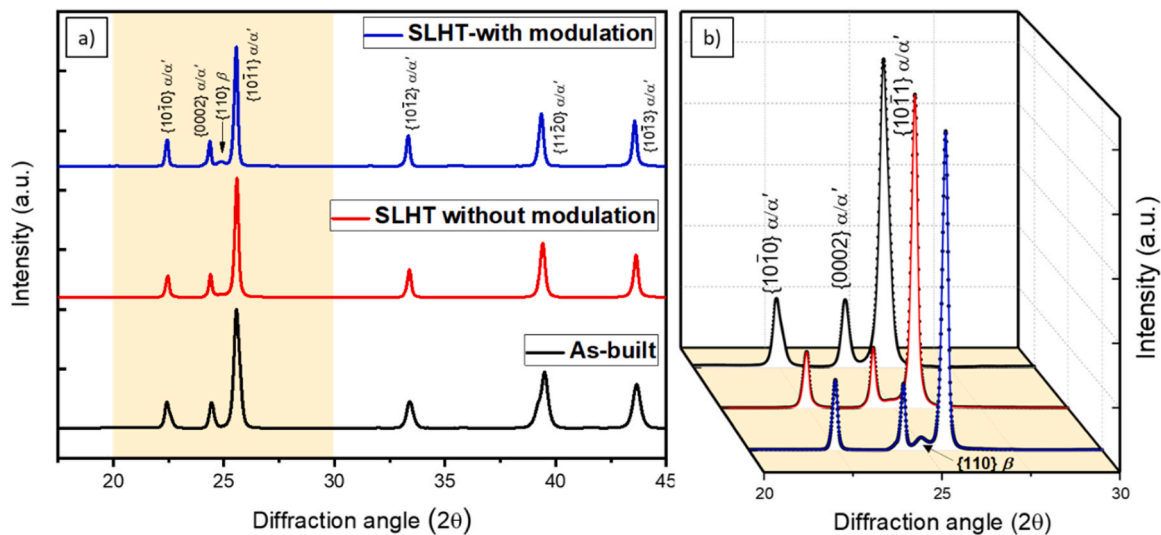


Fig. 5. a) Single XRD pattern acquired from the as-built condition, and after SLHT with and without modulation. b) magnified view of the shaded rectangle in a) in the angular range of 20–30 degrees.

processing, threshold values within the range of $\sim 2900\text{--}6500\text{ K/s}$ have also been considered as the critical value [51]. The measured cooling rate reported in Fig. 4(d) is based on the smoothed curve of the weighted average temperature data taken from Fig. 4(c). The very local cooling rates in each cycle are not experimentally accessible, but can be extracted from the simulations. It is likely that only the lowest cooling rates in the distribution lead to the retained β phase. Even then, our results indicate that the critical cooling rate for fully martensitic structure is beyond $\sim 410\text{ K/s}$.

Ex-situ high resolution diffraction patterns show furthermore that the α/α' peaks are narrower after SLHT for both cases (a) and (b), compared to the as-built state (Fig. 6). For all diffraction planes, the FWHM values after SLHT with modulation (b) are the smallest, whereas the peaks are broadest in the as-built state. The fine structure of the α' -martensite with the presence of micro-strain in the lattice structure explains the observed broadening in the as-built condition [52,53]. Performing SLHT without modulation has also made the peaks narrower compared to the as-built state, albeit, broader with respect to the SLHT with modulation. This can be due to the increased formation of martensite at the end of the SLHT cycles in case (a), causing peak broadening compared to case (b). The removal of the micro strain from the α' -martensitic structure together with the coarsening of the laths is the second additional signature of the α' -martensite decomposition phenomenon into an $\alpha + \beta$ structure [54]. The creation of a site-specific composite structure on the uppermost surface can be readily achieved through this approach which has not been obtained at this scale in the literature. Furthermore, to comprehend the mechanisms of martensite decomposition within the material's depth, a similar methodology (SLHT with the presence of modulation) is also employed to investigate thin wall geometries.

3.2. Thin wall geometry

3.2.1. Numerical simulation

Fig. 7. presents the temperature evolution derived from FEM simulations of the SLHT on a thin wall geometry. The temperature data is plotted at 3 different positions, i.e. $50\text{ }\mu\text{m}$, $150\text{ }\mu\text{m}$, and $250\text{ }\mu\text{m}$ below the top surface of the wall, displayed in blue, red, and black, respectively in Fig. 7. At the beginning of SLHT, the temperature rises rapidly in less than a second, which is followed by a much more gradual increase until the end of the cycles. Employing constant laser parameters until $t \sim 29.2\text{ s}$ has led to a heat build-up in the wall, therefore, the temperature keeps evolving until the end of the SLHT cycle. In order to evaluate local cooling rates, the last SLHT cycles were simulated with fine time

steps, and a magnified view is shown in Fig. 7(b). The green shaded area corresponds to one laser track scanning which lasts $\sim 2.7\text{ ms}$. The weighted average temperature and the temperature fluctuations become smaller as the distance from the top surface increases. Consequently, the local cooling rate ($\partial T/\partial t$) is different depending on the location. Similar to the cuboid geometry case, these findings were used as preliminary studies to perform *operando* SLHT experiments and understand the resulting phase transformation pathway in the depth of a thin wall sample.

3.2.2. Operando experiment

The *operando* experiment on a thin wall geometry is demonstrated in Fig. 8. The gray schematic on the left shows the position of the X-ray with respect to the top surface. For each acquisition, the same SLHT cycles were performed on a freshly printed sample, such as to have similar initial conditions for comparison purposes. The evolution of the diffraction pattern intensity over time is presented as a waterfall plot in Fig. 8(a-c). Similar to the cuboid geometry case, the $\{0002\}_{\alpha/\alpha'}$ and $\{10\bar{1}1\}_{\alpha/\alpha'}$ peaks shifted towards smaller angles upon SLHT due to lattice expansion. Moreover, the $\{011\}_{\beta}$ peak starts appearing at $t \sim 2\text{ s}$ and the intensity becomes increasingly pronounced over time, especially at a depth of $50\text{ }\mu\text{m}$ (Fig. 8(a)). The intensity of the β phase at a depth of $150\text{ }\mu\text{m}$ is reduced (Fig. 8(b)), and at $250\text{ }\mu\text{m}$, only small traces of the β phase remain detectable, mainly at the end of the SLHT cycles. At $t \sim 29.2\text{ s}$, the cooling cycles start, causing peaks shifting towards higher angles. For the thin wall experiments, SLHT was systematically performed with modulation in the last cycles, in order to preserve the decomposed β phase and prevent its reverse transformation to α' -martensite.

The XRD patterns taken after SLHT from *ex-situ* scanning are shown in Fig. 8(d-f), respectively at $50\text{ }\mu\text{m}$, $150\text{ }\mu\text{m}$, and $250\text{ }\mu\text{m}$ underneath the top surface. These were obtained by summing 10 individual patterns acquired at the same depth. It is again noted that more β phase is observed at the position of $50\text{ }\mu\text{m}$, compared to $150\text{ }\mu\text{m}$ and $250\text{ }\mu\text{m}$. Therefore, it can be inferred that the decomposition of the α' -martensite is facilitated at the position of $50\text{ }\mu\text{m}$ compared to the other locations. Moreover, the temperature regime resulted in faster kinetics within the $\sim 30\text{ s}$ at the $50\text{ }\mu\text{m}$ position. To further clarify the kinetics, the temperature field was derived from the changes in the peak shifting and plotted in Fig. 8(g-i), for the three positions of the X-ray beam. Due to the difficulty of the β phase peak tracing, the temperature values were derived by tracking the $\{10\bar{1}1\}_{\alpha/\alpha'}$ peak.

Fig. 8(g) corresponding to the $50\text{ }\mu\text{m}$ position exhibits a sharper slope at the intermediate heating stage, with higher temperatures, compared

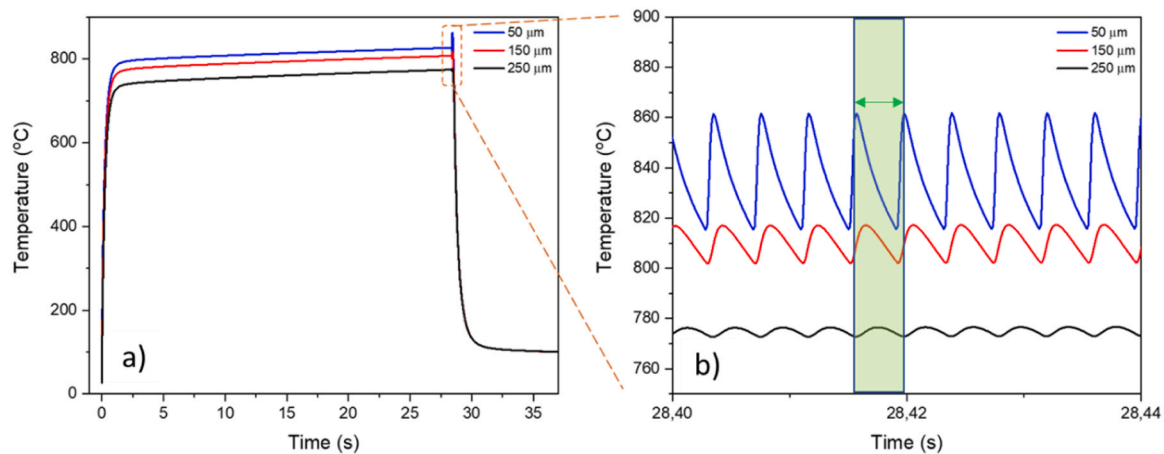


Fig. 7. a) FEM simulation of the temperature evolution at $50\text{ }\mu\text{m}$, $150\text{ }\mu\text{m}$, and $250\text{ }\mu\text{m}$ below the top surface upon SLHT on a thin wall geometry. b) magnified view of the temperature oscillations obtained with fine time steps. The green shaded zone corresponds to one laser track. (For interpretation of the references to color in this figure legend, the reader is referred to the web version of this article.)

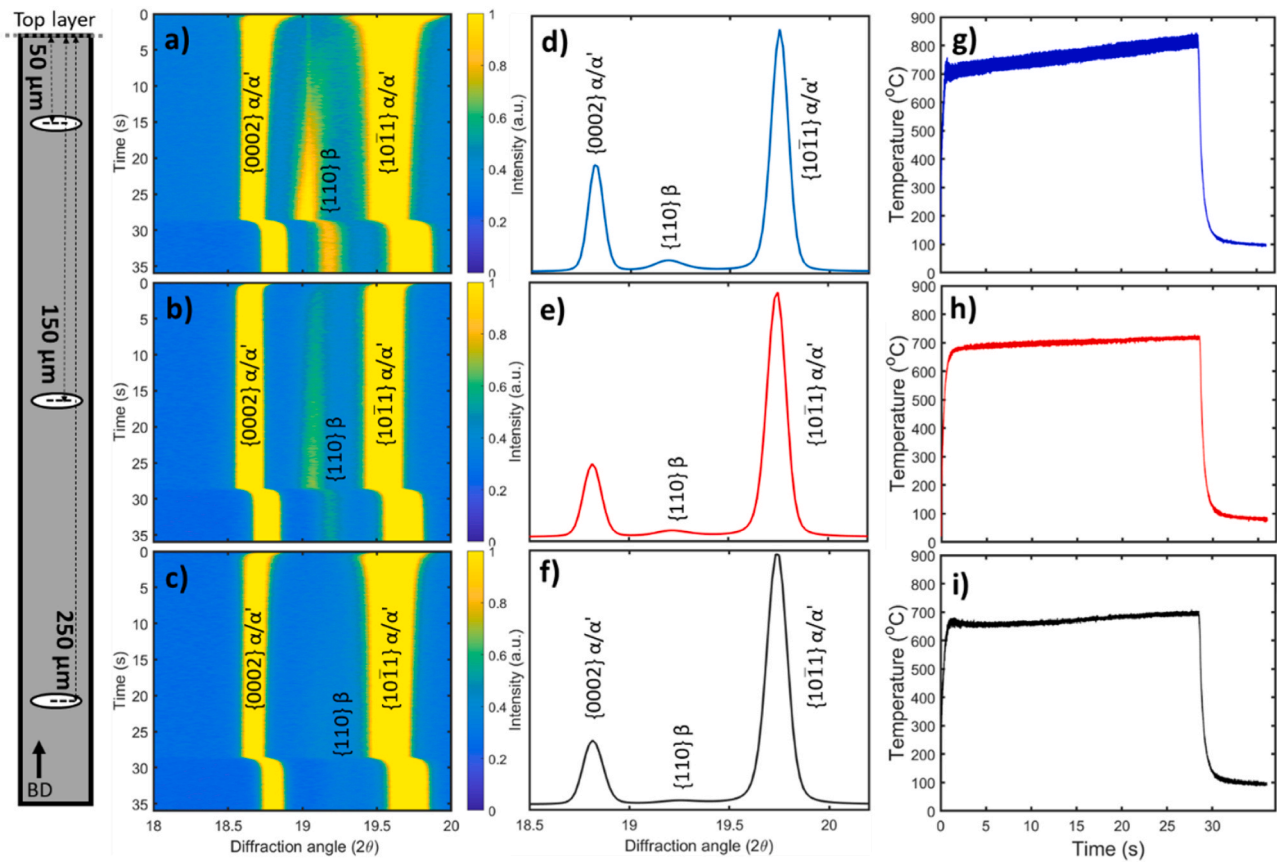


Fig. 8. Operando X-ray diffraction of SLHT on thin wall geometry. The burst mode acquisitions were taken at a) 50 μm , b) 150 μm , and c) 250 μm below the top surface. d-f) single XRD patterns taken at the end of the SLHT cycles by summing 10 individual patterns and g-i) Temperature evolution extracted by peak tracing of the $\{10\bar{1}1\}$ peak of the α/α' phase corresponding to the acquisition position of 50 μm , 150 μm , and 250 μm respectively. The gray scheme on the left represents the positioning of the X-ray beam with respect to the specimen.

to Fig. 8(h) and (i) related to the 150 μm , and 250 μm depths, respectively. The higher average temperature, in the range of 700–830 $^{\circ}\text{C}$, has facilitated α' -martensite decomposition, which is slower at the lower temperatures experienced at the 150 μm and 250 μm positions. Additionally, the temperature oscillations related to laser scanning are more pronounced at the 50 μm position, similarly to the simulation results (Fig. 7(b)), due to the closer distance to the top surface compared to the other locations. The faster kinetics of decomposition near the top surface imply the formation of more β phase and higher chemical composition changes, which means that absolute temperature values may be slightly biased, however the evolution trend derived from the X-ray data and the simulation results are in good agreement. Beside the gradual formation of the β phase, similar to what was observed for the cuboid geometry, narrowing of the α/α' peaks is noticed as the second sign of the decomposition.

As the decomposition is more pronounced at the 50 μm depth, to further investigate the behavior of the α/α' peaks, the evolution of the FWHM at this depth for the first six diffracted planes is shown in Fig. 9. At the very beginning of the SLHT, there is fast a peak broadening, immediately followed by a sharp narrowing and finally an asymptotic decrease. The initial broadening ($t < 0.64$ s) relates to the anisotropic thermal expansion behavior and anisotropic elastic constants of the hexagonal structure [55,56], bringing variable thermal strain in different plane families.

As the decomposition progress, as micro strain is eliminated and the α laths coarsen, all hexagonal peaks gradually become narrower, although to varying degrees. This shows a significant change in the microstructure of hexagonal phase. Note that a small increase in the FWHM at the end of SLHT cycles is also observed. This increase could

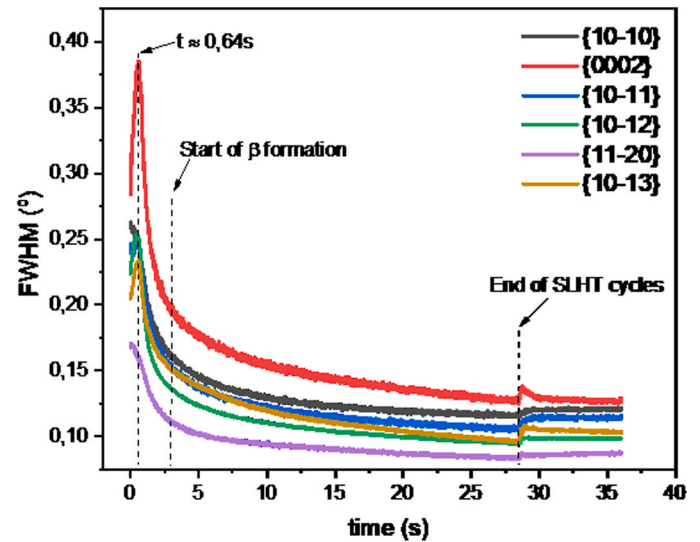


Fig. 9. FWHM evolution in time upon SLHT of the thin wall at 50 μm depth from top layer.

potentially be attributed to partial reverse transformation from β to α' [54,57].

The first attempt to implement laser heat treatment in the LPBF of Ti-6Al-4V has been done by Chen, et al. [58]. Nevertheless, there were no *operando* experiments or simulated data available to provide support for

the findings of this study. Their utilization of laser melting followed by a one-pass laser reheating led to a sandwich structure, composed of a mixture of α , α' , and nano-sized precipitates of the β phases, exhibiting excellent tensile strength (above 1100 MPa) and elongation up to 8 % [58]. Similar approach has also been published for microstructural control in Ti-5553 alloy exhibiting uninterrupted columnar grains [59]. Note that the laser reheating was done at the focal point using low energy density leading to partial re-melting of the top surface. In our work, we measure the dynamics of martensite decomposition and its relatively fast kinetics through the *operando* XRD measurements by means of SLHT within the temperature range of martensite decomposition at relatively lower temperatures with respect to the melting point. The employment of the SLHT can be further explored to any other materials suffering from inferior mechanical properties in the as-built state. However, in the present work, SLHT is only performed on the top surface of the parts. The next step of the SLHT strategy will consist in periodically applying the heat treatment within a 3-dimensional printing process, such as to produce a composite-like microstructure with tailored mechanical properties. The feasibility is demonstrated here, since martensite decomposition can occur at a sufficient distance from the top surface which allows to keep the resulting $\alpha + \beta$ structure when new layers are added.

3.3. Microstructural analysis

Detailed microstructural analysis of the cuboid geometry was performed for case (b) (SLHT with modulation). Fig. 10(a) shows the EBSD map taken from the top surface of the cuboid geometry. The typical lamellar morphology of the hexagonal laths is observable, which has not changed upon the SLHT. The presence of $\sim 4\%$ β (after excluding badly indexed pixels) together with the α phase is evidenced from the EBSD phase color map analysis in Fig. 10(b). The α boundaries are decorated with fine lamellae and particulates of β phase. The EBSD map thus confirms the XRD data. However, the nanometric size of the β phase makes the indexing difficult, which means that the measured volume fraction is probably underestimated.

As explained in Section 3.1.2., there exists some uncertainty in the estimated absolute temperature values. One could assume that if the average temperature (i.e. when smoothing the oscillations) exceeds the β transus over all SLHT cycles, then the β grains should grow compared

to the as-built state. As reported in [60], the duration of existence of the β phase is influenced by the laser processing parameters, which significantly affects the final microstructure. Fig. 11(a) presents an EBSD map of the reconstructed prior β grains in the as-built state, while Fig. 11(b) compares it with after SLHT with modulation (case(b)). Typical rectangular structures arise from the epitaxial growth of the cubic β phase and the 90° rotation of laser scan direction at each layer during the build [60,61]. The average size of the parent grains in c) and d) is $59.1 \pm 4.8 \mu\text{m}$, and $59.4 \pm 6.6 \mu\text{m}$ respectively. Moreover, the morphology of the parent grains remained unchanged. Based on these observations, it can be assumed that through a proper selection of the SLHT processing parameters, the average temperature has indeed remained predominantly below the β transus, in a temperature range favorable to the decomposition of the α' -martensite.

Complementary microstructural analysis via TEM was performed from the cross-sectional view of the top surface of the cuboid after SLHT with modulation in case (b), as shown in Fig. 12. A dual phase lamellar microstructure is clearly visible in the bright field image of Fig. 12(a), suggesting the occurrence of martensite decomposition. To further confirm the elemental partitioning of the dual phase structure, EDS analysis in STEM-HAADF imaging was performed, as illustrated in Fig. 12(b-e). The α boundaries are enriched in V, as shaded in blue in Fig. 12(e), and depleted from Ti and Al, as shown in Fig. 12(c) and (d), respectively. Since V is a β stabilizer, whereas Al is an α stabilizer, this distribution map is expected for a typical dual phase $\alpha + \beta$ lamellar structure as reported in [21]. The enrichment in V at the α boundaries is also supported by the brighter contrast of these regions in STEM-HAADF images (Fig. 12(f)), suggesting the presence of heavier elements. The white areas at the α boundaries, marked with yellow arrows in Fig. 12(g), can thus be considered as extremely fine (~ 10 nm), V-enriched, β lamellae. Note that the short duration of the SLHT did not induce the growth of the β lamellae, which would be desirable for ductility improvement.

The SEM images shown in Fig. 13 represent the cross-sectional views of the thin wall samples taken at the $50 \mu\text{m}$ distance from the top surface. An $\alpha + \beta$ microstructure can be observed in Fig. 13(b, c) whereas the image in Fig. 13(a) exhibits the typical needle shape of the martensite in the as-built state. Therefore, the decomposition has occurred on a greater scale at the $50 \mu\text{m}$ depth as demonstrated by the *operando* diffraction pattern in Fig. 8(d-f) Section 3.2.2. This is

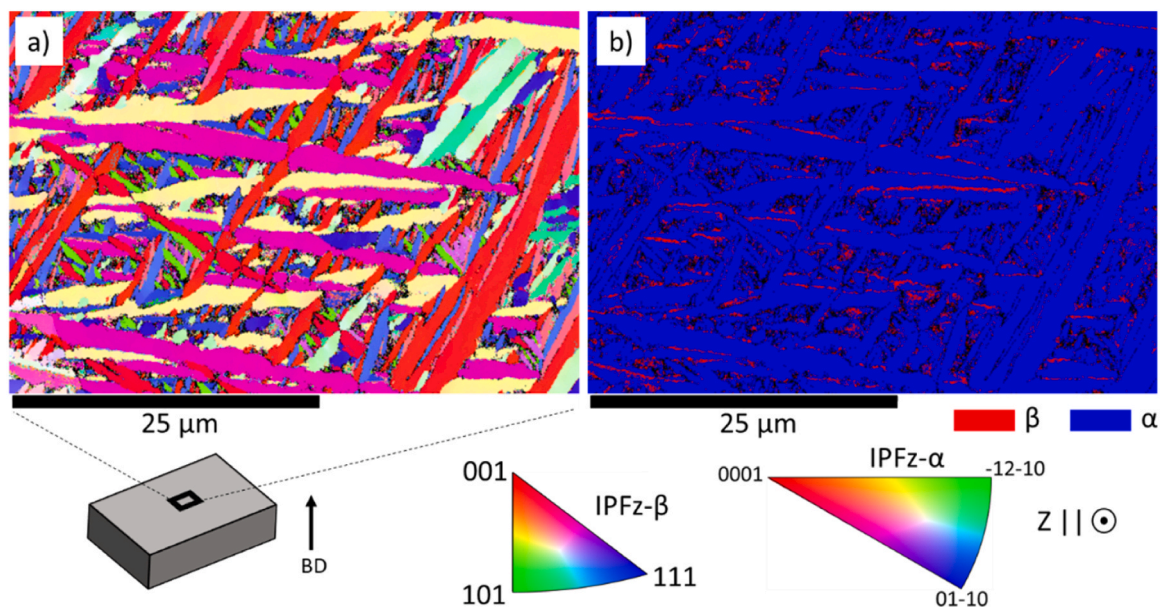


Fig. 10. EBSD a) IPFz, and b) Phase color map taken from the top surface of the cuboid geometry after SLHT with modulation. (For interpretation of the references to color in this figure legend, the reader is referred to the web version of this article.)

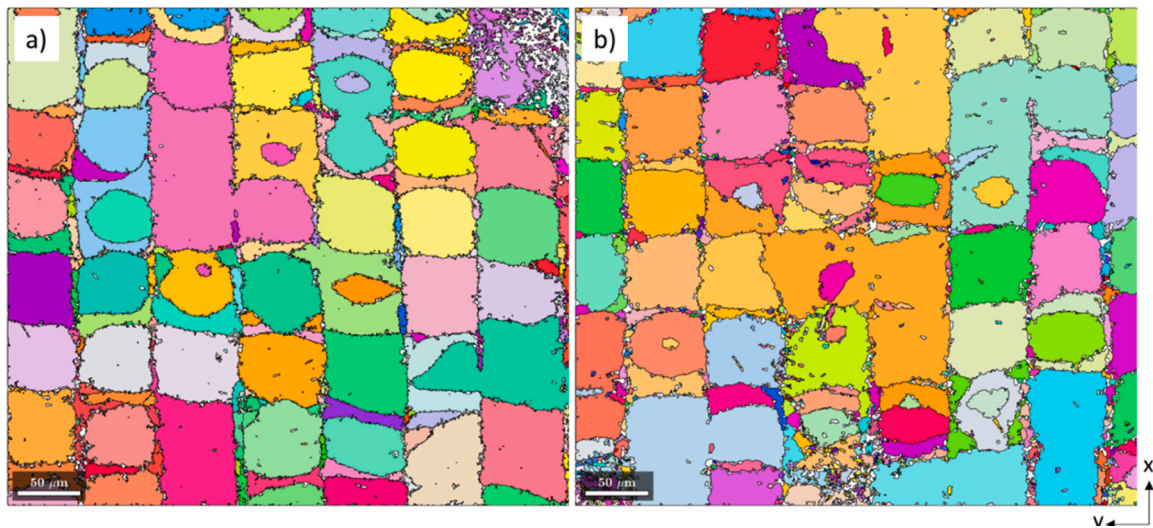


Fig. 11. EBSD reconstructed maps of parent β phase in the a) As-built, and b) SLHT sample. The maps were taken from the top surface.

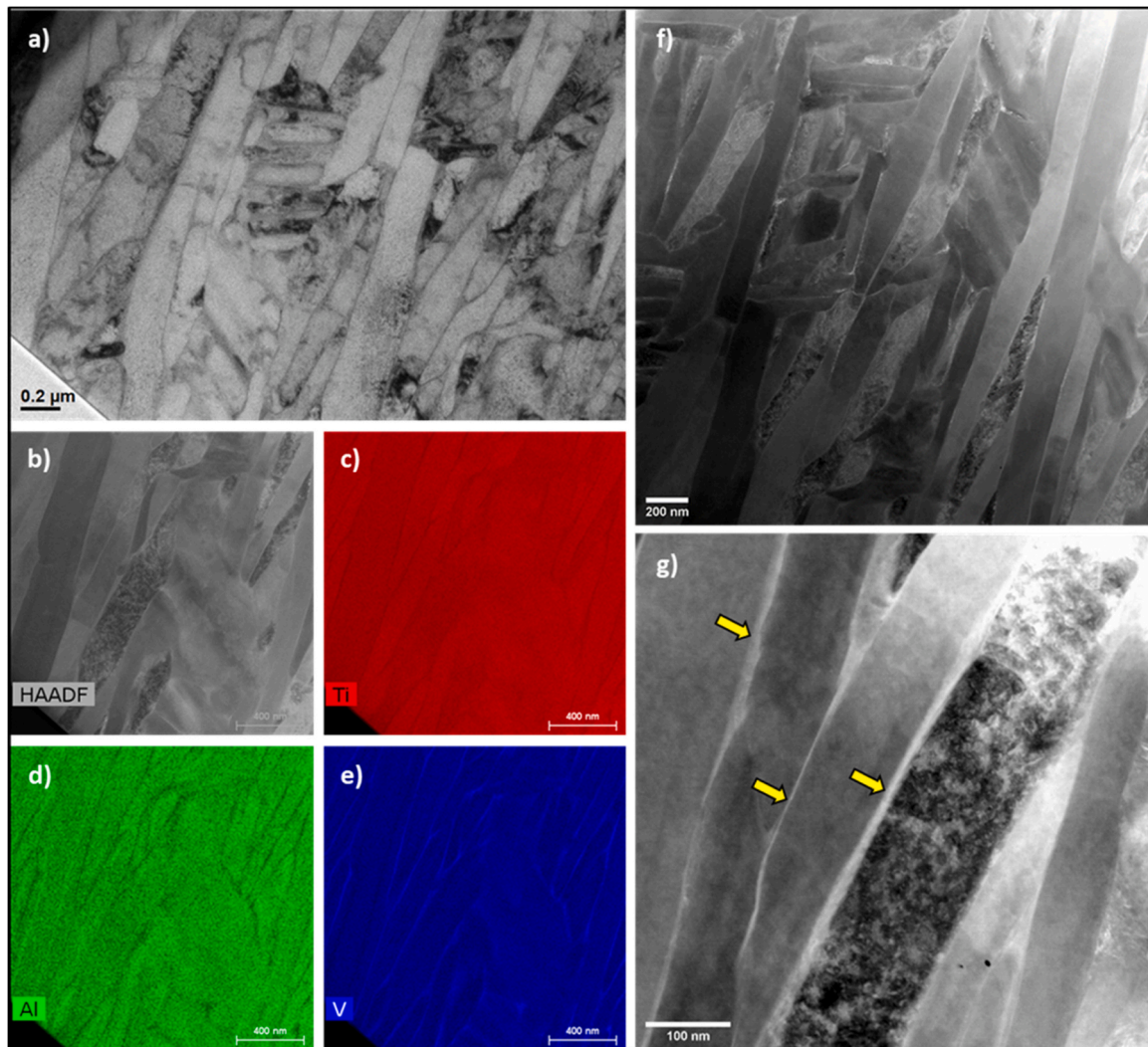


Fig. 12. TEM analysis of the cuboid sample after SLHT with the presence of modulation. a) bright field image of the lamellar structure, b) HAADF, STEM image and its corresponding EDS elemental maps of c) Ti, d) Al, e) V elements. f) and g) STEM-HAADF images of dual phase $\alpha + \beta$ structure.

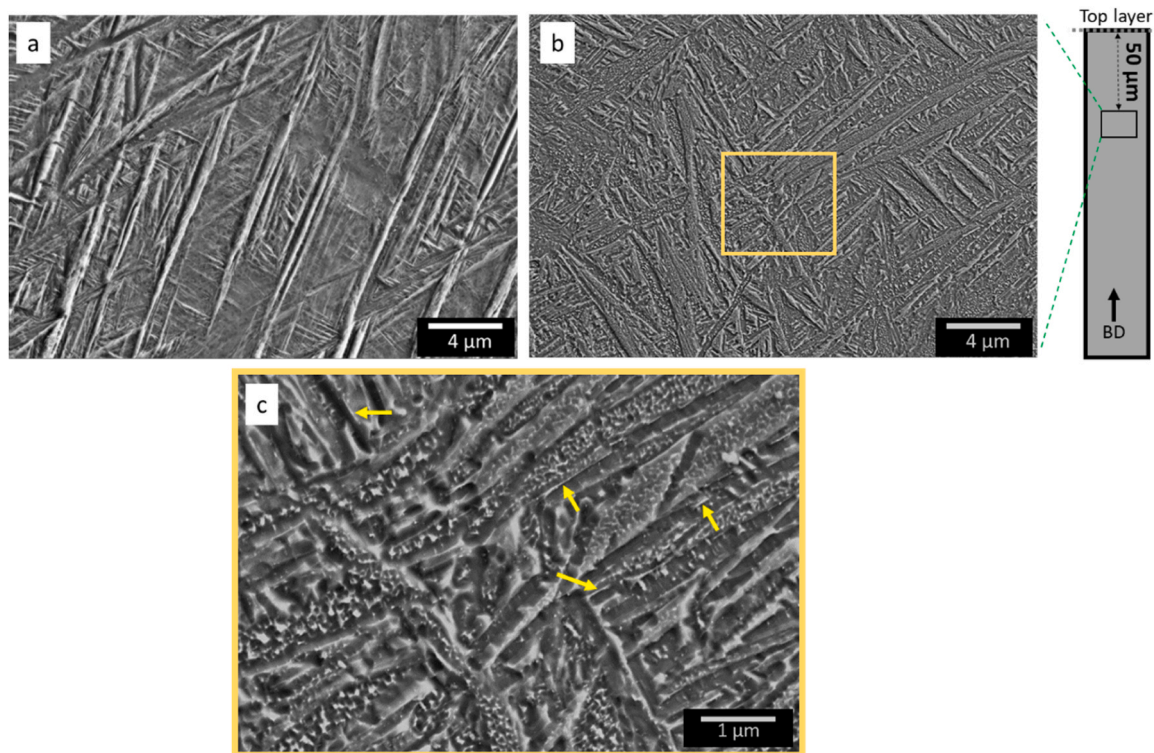


Fig. 13. SEM images of thin wall sample in a) as-built, b), and c) SLHT state taken at the 50 μm below the top surface. The yellow arrows show the bright contrast of the β phase. (For interpretation of the references to color in this figure legend, the reader is referred to the web version of this article.)

attributed to the higher average temperature being experienced at the 50 μm distance from the top compared to the 150 and 250 μm locations. The yellow arrows indicate the β phase rods and particulates based on the previous EBSD and TEM analysis. Therefore, the presence of both particulate and lamellar morphologies implies the existence of decomposition upon short SLHT cycles in the thin wall geometry.

The lamellar $\alpha + \beta$ microstructure in the thin wall geometry may not be as readily discernible suggesting the early stages of decomposition. In Fig. 13(c), we observe some instances of lamellar microstructure along with precipitates of the β phase alongside the acicular α' -martensite. In contrast, the lamellar microstructure on the top surface of a cuboid geometry is evident through TEM analysis in Fig. 12. The observed variation could be attributed to the distinct SLHT parameters, as detailed in Section 2.2, applied to both geometries. This results in different temperature profiles and, in turn, different kinetic behavior at the top surface of the cuboid compared to the 50 μm depth of the thin wall. While our approach did not aim to obtain precise temperature profiles for both cases, it is crucial to underscore the significance of utilizing calibrated numerical simulations for each specific geometry. These simulations allow predicting similar or varying temperature profiles by carefully selecting SLHT parameters, making them an indispensable tool for this research.

4. Conclusion

In this study, we have established an effective strategy for controlling the microstructure of additively manufactured Ti-6Al-4V. The implementation of *in-situ* SLHT has been designed and tested on cuboid and thin wall geometries, through a combination of numerical simulations and *operando* X-ray diffraction measurements. These gave access to the local temperature evolutions, and the dynamics of the α' -martensite decomposition. The following conclusions were obtained:

- Conducting *in-situ* SLHT can effectively induce local microstructural changes in the additively manufactured part, and activate the solid-state phase transformation of $\alpha' \rightarrow \alpha + \beta$ within a short time scale of ~ 30 s.
- Employing a modulation of laser parameters in the last SLHT cycles can drastically change the temperature evolution, and the resulting cooling rate. This strategy allows the preservation of the β phase as a product of the martensite decomposition at a very local scale on the top surface.
- SLHT causes α/α' laths coarsening, resulting in diffraction peaks narrowing of the α/α' .
- Microstructural investigation through EBSD, TEM, and SEM provides additional confirmation on the formation of lamellar $\alpha + \beta$ structure on the top surface of the cuboid geometry and into the depth of thin wall samples.
- The average temperature values and their fluctuations reduce with increasing distance from the top surface of the thin walls. However, the depth at which the martensite decomposes is compatible and can be further tuned with the 3D printing of architected (composite-like) microstructures.

The obtained results suggest furthermore that the calibrated thermal finite element model can be used for the design of *ex-situ* SLHT routes, for any given part geometry. The SLHT approach can also be explored on other materials, for optimizing the LPBF as-built properties through local microstructure tailoring.

CRediT authorship contribution statement

Reza Esmailzadeh: Writing – original draft, Validation, Methodology, Investigation, Formal analysis, Conceptualization. **Milad Hamidi-Nasab:** Writing – review & editing, Validation, Methodology, Formal analysis, Conceptualization. **Charlotte de Formanoir:** Writing – review & editing, Validation, Methodology, Investigation, Formal

analysis. **Lucas Schlenger**: Writing – review & editing, Investigation, Formal analysis, Data curation. **Steven Van Petegem**: Validation, Resources, Methodology, Formal analysis, Data curation, Funding acquisition, Writing - review & editing. **Claire Navarre**: Visualization, Validation, Formal analysis. **Cyril Cayron**: Writing – review & editing, Validation, Methodology, Formal analysis. **Nicola Casati**: Visualization, Resources, Data curation. **Daniel Grolimund**: Visualization, Resources, Formal analysis. **Roland E. Logé**: Writing – review & editing, Supervision, Resources, Project administration, Funding acquisition.

Declaration of Competing Interest

The authors declare that they have no known competing financial interests or personal relationships that could have appeared to influence the work reported in this paper.

Data availability

Data will be made available on request.

Acknowledgements

The authors acknowledge financial support from the Swiss National Science Foundation (SNSF project No. CRSII5_193799). We also acknowledge the Paul Scherrer Institut (PSI) for the provision of synchrotron beamtime at MS and MicroXAS beamline at Swiss Light Source (SLS) under the proposal number 20212101 and 20212136. The generous financial support from PX-group to LMTM is appreciated. We also thank Barbora Bártová for her assistance on TEM lamella preparation at CMi center at EPFL as well as Mathijs van der Meer for his technical support.

Appendix A. Supporting information

Supplementary data associated with this article can be found in the online version at [doi:10.1016/j.addma.2023.103882](https://doi.org/10.1016/j.addma.2023.103882).

References

- [1] I. Bahrini, M. Rivette, A. Rechia, A. Siadat, A. Elmesbahi, Additive manufacturing technology: the status, applications, and prospects, *Int. J. Adv. Manuf. Technol.* 97 (2018) 147–161, <https://doi.org/10.1007/s00170-018-1932-y>.
- [2] T. DebRoy, H.L. Wei, J.S. Zuback, T. Mukherjee, J.W. Elmer, J.O. Milewski, A. M. Beese, A. Wilson-Heid, A. De, W. Zhang, Additive manufacturing of metallic components – Process, structure and properties, *Prog. Mater. Sci.* 92 (2018) 112–224, <https://doi.org/10.1016/j.pmatsci.2017.10.001>.
- [3] D. Herzog, V. Seyda, E. Wycisk, C. Emmelmann, Additive manufacturing of metals, *Acta Mater.* 117 (2016) 371–392, <https://doi.org/10.1016/j.actamat.2016.07.019>.
- [4] A. Gisario, M. Kazarian, F. Martina, M. Mehrpouya, Metal additive manufacturing in the commercial aviation industry: a review, *J. Manuf. Syst.* 53 (2019) 124–149, <https://doi.org/10.1016/j.jmsys.2019.08.005>.
- [5] A. Sola, A. Nouri, Microstructural porosity in additive manufacturing: the formation and detection of pores in metal parts fabricated by powder bed fusion, *J. Adv. Manuf. Process* 1 (2019), <https://doi.org/10.1002/amp.2.10021>.
- [6] W.S.W. Harun, M.S.I.N. Kamariah, N. Muhamad, S.A.C. Ghani, F. Ahmad, Z. Mohamed, A review of powder additive manufacturing processes for metallic biomaterials, *Powder Technol.* 327 (2018) 128–151, <https://doi.org/10.1016/j.powtec.2017.12.058>.
- [7] M. Niinomi, Mechanical biocompatibilities of titanium alloys for biomedical applications, *J. Mech. Behav. Biomed. Mater.* 1 (2008) 30–42, <https://doi.org/10.1016/j.jmbbm.2007.07.001>.
- [8] Y. Zhu, J. Zou, H. yong Yang, Wear performance of metal parts fabricated by selective laser melting: a literature review, *J. Zhejiang Univ. Sci. A* 19 (2018) 95–110, <https://doi.org/10.1631/jzus.A1700328>.
- [9] M. Motyka, K. Kubiak, J. Sieniawski, W. Ziaja, Phase transformations and characterization of $\alpha + \beta$ titanium alloys. in: *Comprehensive Materials Processing*, Elsevier Ltd, 2014, pp. 7–36, <https://doi.org/10.1016/B978-0-08-096532-1.00202-8>.
- [10] S. Liu, Y.C. Shin, Additive manufacturing of Ti6Al4V alloy: a review, *Mater. Des.* 164 (2019), <https://doi.org/10.1016/j.matdes.2018.107552>.
- [11] A.K. Singla, M. Banerjee, A. Sharma, J. Singh, A. Bansal, M.K. Gupta, N. Khanna, A. S. Shahi, D.K. Goyal, Selective laser melting of Ti6Al4V alloy: process parameters, defects and post-treatments, *J. Manuf. Process* 64 (2021) 161–187, <https://doi.org/10.1016/j.jmapro.2021.01.009>.
- [12] B. Wysocki, P. Maj, R. Sitek, J. Buhagiar, K.J. Kurzydowski, W. Świeszkowski, Laser and electron beam additive manufacturing methods of fabricating titanium bone implants, *Appl. Sci.* 7 (2017), <https://doi.org/10.3390/app7070657>.
- [13] H.K. Rafi, N. v Karthik, H. Gong, T.L. Starr, B.E. Stucker, Microstructures and mechanical properties of Ti6Al4V parts fabricated by selective laser melting and electron beam melting, *J. Mater. Eng. Perform.* 22 (2013) 3872–3883, <https://doi.org/10.1007/s11665-013-0658-0>.
- [14] G. Kasperovich, J. Hausmann, Improvement of fatigue resistance and ductility of TiAl6V4 processed by selective laser melting, *J. Mater. Process Technol.* 220 (2015) 202–214, <https://doi.org/10.1016/j.jmatprotec.2015.01.025>.
- [15] T. Vilaro, C. Colin, J.D. Bartout, As-fabricated and heat-treated microstructures of the Ti-6Al-4V alloy processed by selective laser melting, *Met. Mater. Trans. A Phys. Met. Mater. Sci.* 42 (2011) 3190–3199, <https://doi.org/10.1007/s11661-011-0731-y>.
- [16] W. Xu, M. Brandt, S. Sun, J. Elambasseril, Q. Liu, K. Latham, K. Xia, M. Qian, Additive manufacturing of strong and ductile Ti-6Al-4V by selective laser melting via in situ martensite decomposition, *Acta Mater.* 85 (2015) 74–84, <https://doi.org/10.1016/j.actamat.2014.11.028>.
- [17] W. Xu, E.W. Lui, A. Pateras, M. Qian, M. Brandt, In situ tailoring microstructure in additively manufactured Ti-6Al-4V for superior mechanical performance, *Acta Mater.* 125 (2017) 390–400, <https://doi.org/10.1016/j.actamat.2016.12.027>.
- [18] P. Barriobero-Vila, J. Gussone, J. Haubrich, S. Sandlöbes, J.C. da Silva, P. Cloetens, N. Schell, G. Requena, Inducing stable $\alpha + \beta$ microstructures during selective laser melting of Ti-6Al-4V using intensified intrinsic heat treatments, *Materials* 10 (2017), <https://doi.org/10.3390/ma10030268>.
- [19] A. Zafari, M.R. Barati, K. Xia, Controlling martensitic decomposition during selective laser melting to achieve best ductility in high strength Ti-6Al-4V, *Mater. Sci. Eng. A* 744 (2019) 445–455, <https://doi.org/10.1016/j.msea.2018.12.047>.
- [20] J. Chen, D. Fabijanic, T. Zhang, E.W. Lui, M. Brandt, W. Xu, Deciphering the transformation pathway in laser powder-bed fusion additive manufacturing of Ti-6Al-4V alloy, *Addit. Manuf.* 58 (2022), 103041, <https://doi.org/10.1016/j.addma.2022.103041>.
- [21] H. Wang, Q. Chao, H.S. Chen, Z.B. Chen, S. Primig, W. Xu, S.P. Ringer, X.Z. Liao, Formation of a transition V-rich structure during the α' to $\alpha + \beta$ phase transformation process in additively manufactured Ti-6Al-4 V, *Acta Mater.* 235 (2022), <https://doi.org/10.1016/j.actamat.2022.118104>.
- [22] X. Yang, R.A. Barrett, M. Tong, N.M. Harrison, S.B. Leen, Towards a process-structure model for Ti-6Al-4V during additive manufacturing, *J. Manuf. Process* 61 (2021) 428–439, <https://doi.org/10.1016/j.jmapro.2020.11.033>.
- [23] E. Salsi, M. Chiumenti, M. Cervera, Modeling of microstructure evolution of Ti6Al4V for additive manufacturing, *Metals* 8 (2018), <https://doi.org/10.3390/met8080633>.
- [24] S. Hocine, H. van Swygenhoven, S. van Petegem, C.S.T. Chang, T. Maimaitiylili, G. Tinti, D. Ferreira Sanchez, D. Grolimund, N. Casati, Operando X-ray diffraction during laser 3D printing, *Mater. Today* 34 (2020) 30–40, <https://doi.org/10.1016/j.mattod.2019.10.001>.
- [25] H. Ghasemi-Tabasi, C. de Formanoir, S. van Petegem, J. Jhabvala, S. Hocine, E. Boillat, N. Sohrabi, F. Marone, D. Grolimund, H. van Swygenhoven, R.E. Logé, Direct observation of crack formation mechanisms with operando laser powder bed fusion X-ray imaging, *Addit. Manuf.* 51 (2022), <https://doi.org/10.1016/j.addma.2022.102619>.
- [26] T. Sun, W. Tan, L. Chen, A. Rollett, In situ/operando synchrotron x-ray studies of metal additive manufacturing, *MRS Bull.* 45 (2020) 927–933, <https://doi.org/10.1557/mrs.2020.275>.
- [27] C. Ioannidou, H.-H. König, N. Semjatov, U. Ackelid, P. Staron, C. Körner, P. Hedström, G. Lindwall, In-situ synchrotron X-ray analysis of metal additive manufacturing: current state, opportunities and challenges, *Mater. Des.* 219 (2022), 110790, <https://doi.org/10.1016/j.matdes.2022.110790>.
- [28] V. Thampy, A.Y. Fong, N.P. Caltia, J. Wang, A.A. Martin, P.J. Depond, A.M. Kiss, G. Guss, Q. Xing, R.T. Ott, A. van Buuren, M.F. Toney, J.N. Weker, M.J. Kramer, M. J. Matthews, C.J. Tassone, K.H. Stone, Subsurface cooling rates and microstructural response during laser based metal additive manufacturing, *Sci. Rep.* 10 (2020), <https://doi.org/10.1038/s41598-020-58598-z>.
- [29] M. Chen, M. Simonelli, S. Van Petegem, Y. Yau Tse, C. Sin Ting Chang, M. Grazyna Makowska, D. Ferreira Sanchez, H. Moens-Van Swygenhoven, A quantitative study of thermal cycling along the build direction of Ti-6Al-4V produced by laser powder bed fusion, *Mater. Des.* 225 (2023), <https://doi.org/10.1016/j.matdes.2022.111458>.
- [30] M. Chen, S. Van Petegem, Z. Zou, M. Simonelli, Y.Y. Tse, C.S.T. Chang, M. G. Makowska, D. Ferreira Sanchez, H. Moens-Van Swygenhoven, Microstructural engineering of a dual-phase Ti-Al-V-Fe alloy via in situ alloying during laser powder bed fusion, *Addit. Manuf.* 59 (2022), <https://doi.org/10.1016/j.addma.2022.103173>.
- [31] S.L. Lu, C.J. Todaro, Y.Y. Sun, T. Song, M. Brandt, M. Qian, Variant selection in additively manufactured alpha-beta titanium alloys, *J. Mater. Sci. Technol.* 113 (2022) 14–21, <https://doi.org/10.1016/j.jmst.2021.10.021>.
- [32] S. Hocine, S. Van Petegem, U. Frommherz, G. Tinti, N. Casati, D. Grolimund, H. Van Swygenhoven, A miniaturized selective laser melting device for operando X-ray diffraction studies, *Addit. Manuf.* 34 (2020), <https://doi.org/10.1016/j.addma.2020.101194>.
- [33] W.E. King, H.D. Barth, V.M. Castillo, G.F. Gallegos, J.W. Gibbs, D.E. Hahn, C. Kamath, A.M. Rubenchik, Observation of keyhole-mode laser melting in laser powder-bed fusion additive manufacturing, *J. Mater. Process Technol.* 214 (2014) 2915–2925, <https://doi.org/10.1016/j.jmatprotec.2014.06.005>.

- [34] D.B. Hann, J. Iammi, J. Folkes, A simple methodology for predicting laser-weld properties from material and laser parameters, *J. Phys. D Appl. Phys.* 44 (2011), <https://doi.org/10.1088/0022-3727/44/44/445401>.
- [35] H. Ghasemi-Tabasi, J. Jhabvala, E. Boillat, T. Ivas, R. Drissi-Daoudi, R.E. Logé, An effective rule for translating optimal selective laser melting processing parameters from one material to another, *Addit. Manuf.* 36 (2020), <https://doi.org/10.1016/j.addma.2020.101496>.
- [36] M. Boivineau, C. Cagran, D. Doytier, V. Eyraud, M.H. Nadal, B. Wilthan, G. Pottlacher, Thermophysical properties of solid and liquid Ti-6Al-4V (TA6V) alloy, *Int. J. Thermophys.* 27 (2006) 507–529, <https://doi.org/10.1007/PL00021868>.
- [37] J.J.Z. Li, W.L. Johnson, W.K. Rhim, Thermal expansion of liquid Ti-6Al-4V measured by electrostatic levitation, *Appl. Phys. Lett.* 89 (2006), <https://doi.org/10.1063/1.2349840>.
- [38] N. Milošević, I. Aleksić, Thermophysical properties of solid phase Ti-6Al-4V alloy over a wide temperature range, *Int. J. Mater. Res.* (2012) 707–714, <https://doi.org/10.3139/146.110678>.
- [39] G. Tinti, A. Bergamaschi, S. Cartier, R. Dinapoli, D. Greiffenberg, I. Johnson, J. H. Jungmann-Smith, D. Mezza, A. Mozzanica, B. Schmitt, X. Shi, Performance of the EIGER single photon counting detector, *J. Instrum.* 10 (2015), <https://doi.org/10.1088/1748-0221/10/03/C03011>.
- [40] G. Ashiotis, A. Deschildre, Z. Nawaz, J.P. Wright, D. Karkoulis, F.E. Picca, J. Kieffer, The fast azimuthal integration Python library: PyFAI, *J. Appl. Crystallogr.* 48 (2015) 510–519, <https://doi.org/10.1107/S1600576715004306>.
- [41] Y.S. Touloukian, R.K. Kirby, R.E. Taylor, P.D. Desai, *Thermal Expansion: Metallic Elements and alloys*, Springer, Boston, 1975, <https://doi.org/10.1007/978-1-4757-1622-1>.
- [42] Q. Zhang, J. Xie, Z. Gao, T. London, D. Griffiths, V. Oancea, A metallurgical phase transformation framework applied to SLM additive manufacturing processes, *Mater. Des.* 166 (2019), <https://doi.org/10.1016/j.matdes.2019.107618>.
- [43] K.C. Mills, *Thermophysical Properties for Selected Commercial Alloys*, Woodhead, Cambridge, 2002.
- [44] E. Rodriguez, J. Mireles, C.A. Terrazas, D. Espalin, M.A. Perez, R.B. Wicker, Approximation of absolute surface temperature measurements of powder bed fusion additive manufacturing technology using in situ infrared thermography, *Addit. Manuf.* 5 (2015) 31–39, <https://doi.org/10.1016/j.addma.2014.12.001>.
- [45] M. Masoomi, J.W. Pegues, S.M. Thompson, N. Shamsaei, A numerical and experimental investigation of convective heat transfer during laser-powder bed fusion, *Addit. Manuf.* 22 (2018) 729–745, <https://doi.org/10.1016/j.addma.2018.06.021>.
- [46] F. Niessen, T. Nyyssönen, A.A. Gazder, R. Hielscher, Parent grain reconstruction from partially or fully transformed microstructures in MTEX, *J. Appl. Crystallogr.* 55 (2022) 180–194, <https://doi.org/10.1107/S1600576721011560>.
- [47] T. Ahmed, H.J. Rack, *Phase Transformations during Cooling in H + Ti Titanium Alloys*, 1998.
- [48] C. Zhao, K. Fezzaa, R.W. Cunningham, H. Wen, F. de Carlo, L. Chen, A.D. Rollett, T. Sun, Real-time monitoring of laser powder bed fusion process using high-speed X-ray imaging and diffraction, *Sci. Rep.* 7 (2017), <https://doi.org/10.1038/s41598-017-03761-2>.
- [49] S.L. Semiatin, S.L. Knisley, P.N. Fagin, F. Zhang, D.R. Barker, Microstructure Evolution during Alpha-Beta Heat Treatment of Ti-6Al-4V, n.d.
- [50] J. Yang, H. Yu, J. Yin, M. Gao, Z. Wang, X. Zeng, Formation and control of martensite in Ti-6Al-4V alloy produced by selective laser melting, *Mater. Des.* 108 (2016) 308–318, <https://doi.org/10.1016/j.matdes.2016.06.117>.
- [51] S.A. Oh, R.E. Lim, J.W. Aroh, A.C. Chuang, B.J. Gould, B. Amin-Ahmadi, J. v Bernier, T. Sun, P.C. Pistorius, R.M. Suter, A.D. Rollett, High speed synchrotron X-ray diffraction experiments resolve microstructure and phase transformation in laser processed Ti-6Al-4V, *Mater. Res. Lett.* 9 (2021) 429–436, <https://doi.org/10.1080/21663831.2021.1966537>.
- [52] J.M. Vallejos, P. Barriobero-Vila, J. Gussone, J. Haubrich, K. Kelm, A. Stark, N. Schell, G. Requena, In situ high-energy synchrotron X-ray diffraction reveals the role of texture on the activation of slip and twinning during deformation of laser powder bed fusion Ti-6Al-4V, *Adv. Eng. Mater.* 23 (2021), <https://doi.org/10.1002/adem.202001556>.
- [53] J.W. Elmer, T.A. Palmer, S.S. Babu, E.D. Specht, In situ observations of lattice expansion and transformation rates of α and β phases in Ti-6Al-4V, *Mater. Sci. Eng. A* 391 (2005) 104–113, <https://doi.org/10.1016/j.msea.2004.08.084>.
- [54] D.W. Brown, V. Anghel, L. Balogh, B. Clausen, N.S. Johnson, R.M. Martinez, D. C. Pagan, G. Rafailov, L. Ravkov, M. Strantz, E. Zepeda-Alarcon, Evolution of the microstructure of laser powder bed fusion Ti-6Al-4V during post-build heat treatment, *Met. Mater. Trans. A Phys. Met. Mater. Sci.* 52 (2021) 5165–5181, <https://doi.org/10.1007/s11661-021-06455-7>.
- [55] R.E. Lim, D.C. Pagan, D.E. Boyce, J. v Bernier, P.A. Shade, A.D. Rollett, Grain-resolved temperature-dependent anisotropy in hexagonal Ti-7Al revealed by synchrotron X-ray diffraction, *Mater. Charact.* 174 (2021), <https://doi.org/10.1016/j.matchar.2021.110943>.
- [56] Z. Zheng, P. Eisenlohr, T.R. Bieler, D.C. Pagan, F.P.E. Dunne, Heterogeneous internal strain evolution in commercial purity titanium due to anisotropic coefficients of thermal expansion, *JOM* 72 (2020) 39–47, <https://doi.org/10.1007/s11837-019-03743-x>.
- [57] D. Zhang, L. Wang, H. Zhang, A. Maldar, G. Zhu, W. Chen, J.S. Park, J. Wang, X. Zeng, Effect of heat treatment on the tensile behavior of selective laser melted Ti-6Al-4V by in situ X-ray characterization, *Acta Mater.* 189 (2020) 93–104, <https://doi.org/10.1016/j.actamat.2020.03.003>.
- [58] X. Chen, C. Qiu, In-situ development of a sandwich microstructure with enhanced ductility by laser reheating of a laser melted titanium alloy, *Sci. Rep.* 10 (2020), <https://doi.org/10.1038/s41598-020-72627-x>.
- [59] M. Hasanabadi, A. Keshavarzkermai, H. Asgari, N. Azizi, A. Gerlich, E. Toyserkani, In-situ microstructure control by laser post-exposure treatment during laser powder-bed fusion, *Addit. Manuf. Lett.* 4 (2023), 100110, <https://doi.org/10.1016/j.addlet.2022.100110>.
- [60] S. Hocine, H. Van Swygenhoven, S. Van Petegem, C.S.T. Chang, T. Maimaitiyili, G. Tinti, D. Ferreira Sanchez, D. Grolmund, N. Casati, Operando X-ray diffraction during laser 3D printing, *Mater. Today* 34 (2020) 30–40, <https://doi.org/10.1016/j.mattod.2019.10.001>.
- [61] C. Pazuon, S. van Petegem, E. Hryha, C. Sin Ting Chang, S. Hocine, H. van Swygenhoven, C. de Formanoir, S. Dubiez-Le Goff, Effect of helium as process gas on laser powder bed fusion of Ti-6Al-4V studied with operando diffraction and radiography, *Eur. J. Mater.* 2 (2022) 422–435, <https://doi.org/10.1080/26889277.2022.2081622>.